Pressure Induced Enhancement of Thermoelectric Figure of Merit and Structural Phase Transitions in TiNiSn

*Jason L. Baker[1], Changyong Park[2], Curtis Kenney-Benson[2], Vineet Kumar Sharma[3], V. Kanchana [3], G. Vaitheeswaran[4], Chris J Pickard[5], Andrew Cornelius[6], Nenad Velisavljevic[2,7], and Ravhi S. Kumar[6,8**]*

[1]*Earth and Environmental Sciences Division, Los Alamos National Laboratory, Los Alamos, New Mexico 87545, United States*

[2]*High Pressure Collaborative Access Team, X-ray Science Division, Argonne National Laboratory, Argonne, Illinois 60439, USA*

[3]*Department of Physics, Indian Institute of Technology Hyderabad, Kandi Sanga Reddy 502 285, Telengana, India*

[4]*School of Physics, University of Hyderabad, Prof. C. R. Rao Road, Gachibowli, Hyderabad 500 046, Telengana, India*

[5]*Department of Materials Science and Metallurgy, University of Cambridge, Cambridge, UK*

[6]*Department of Physics, University of Nevada Las Vegas, 4505 Maryland Pkwy, Las Vegas, NV 89054, USA.*

[7]*Physics Division, Lawrence Livermore National Laboratory, Livermore, CA 94550, USA*

[8]*Department of Physics, University of Illinois at Chicago, 845 West Taylor Street, Chicago, IL 60607, USA*

AUTHOR INFORMATION

Corresponding Author

**Ravhi S. Kumar: ravhi@uic.edu

ABSTRACT

Half-Heusler thermoelectric materials are potential candidates for high thermoelectric efficiency. We report high-pressure thermoelectric, structural property measurements, density functional theory calculations on the half-Heusler material TiNiSn, and an increase of 15% in the relative dimensionless figure of merit, ZT, around 3 GPa. Thermal and electrical properties were measured utilizing a specialized sample cell assembly designed for the Paris-Edinburgh large-volume press to a maximum pressure of 3.5 GPa. High-pressure structural measurements performed up to 50 GPa in a diamond-anvil cell indicated the emergence of a new high-pressure phase around 20 GPa. A first principles structure search performed using an ab initio random structure search approach identified the high-pressure phase as an orthorhombic type, in good agreement with the experimental results.

TOC GRAPHICS

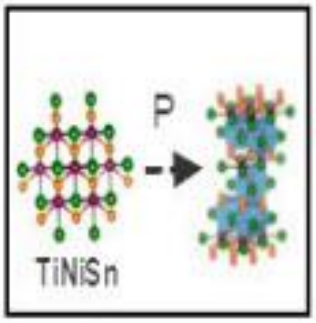

As global energy production continually increases, it becomes of ever-increasing importance to research, identify, synthesize, and characterize materials that can provide a renewable and reliable source of energy and waste heat recovery.[1] One such class of materials are thermoelectric materials, which enable the conversion of heat energy via a thermal gradient into electrical energy without a reliance on moving parts. Thermoelectric materials have long provided industrial energy solutions for specific applications, such as power through radio-isotope thermoelectric generators used by NASA on several space-faring missions.[2] Although these materials have the potential to provide a reliable method of energy production and reduction of waste heat energy, their practical application is highly dependent on their efficiency. This efficiency is defined through a dimensionless figure of merit (ZT):

$$\boldsymbol{ZT} = \frac{\boldsymbol{\alpha^2\sigma}}{\boldsymbol{\kappa}}\boldsymbol{T} \quad (1)$$

where α, σ, T, κ are the Seebeck coefficient, electrical conductivity, absolute temperature, and the thermal conductivity, respectively. A larger value for ZT indicates a material with a greater thermoelectric efficiency. As Equation 1 implies, a larger efficiency (at a constant temperature) strongly depends on having a large Seebeck coefficient, a high electrical conductivity, and a low thermal conductivity.

Several classes of thermoelectric materials are of high-interest such as half-Heusler compounds,[3-9] filled skutterdites,[10,11] nano-structured alloys,[11,12] binary chalcogenides,[13,14] and others.[15-17] Of particular interest among these classes of materials are the half-Heusler compounds due to their typically high Seebeck coefficient and generally good electrical conductivity.[3-9] However, these materials tend to have fairly large thermal

conductivity, which according to Equation 1, would decrease ZT in these materials. Research has been dedicated to identifying methods to reduce the thermal conductivity of these materials while ideally retaining or increasing the Seebeck coefficient and electrical conductivity. The MNiSn family of half-Heusler alloys has been extensively studied with the goal set to increase their ZT value.[18-22] These materials exhibit a very high Seebeck coefficient at room temperature conditions, reaching values of over -200 μV/K.[19-24] Bhattacharya *et al*. have reported an increase in the power factor ($\sigma \cdot \alpha^2$) with a small amount of Sb doping at the Sn site of TiNiSn through a large decrease in the electrical resistivity despite a decrease in the Seebeck coefficient.[19] Other studies have showed a strong effect on the thermoelectric properties during the synthesis process when performing spark plasma sintering (SPS) at various temperatures.[21] Kurosaki *et al*. performed SPS on $(Zr_{0.6}Hf_{0.4})_{0.7}Ti_{0.3}NiSn$ at 973 K, 1173 K, and 1373 K and observed optimal thermoelectric efficiency in the sample prepared at 1173 K.[21] Even though a decrease was reported in the power factor, a decrease of 70% in the thermal conductivity leads to a ZT value of 0.43 at 760 K.[21] Similar to other half-Heusler compounds, MNiSn exhibits large thermal conductivity and without proper reduction of these large values, their applicability to devices is limited.

To further optimize the thermoelectric efficiency of these materials, continued effort is required to identify and characterize new phases and understand the transport behavior in a variety of conditions (i.e., temperature, pressure). Both pressure and temperature can significantly alter the thermal, electrical and structural properties of materials and specifically have a positive effect on thermoelectric efficiency in several studies.[25-29] PbTe and other chalcogenides have shown large changes in electrical resistivity and power factor with application of modest pressures.[25] Recently, Baker *et al*. studied the thermoelectric behavior of

SnTe at high-pressure conditions and observed a significant increase in Seebeck coefficient over the pressure range studied. Due to potential access to high-pressure phases and unique behavior of materials under high-pressure conditions, studying the electrical, thermal and structural properties of TiNiSn as a function of pressure is important.

The high-pressure structural and thermoelectric behavior of TiNiSn has not been investigated experimentally. For the importance of pressure as a method for tuning the transport properties of materials and identifying new phases of materials with potentially favorable thermoelectric properties, it is imperative to study this material at high P-T conditions. Theoretical studies have been conducted by Wang *et al*. and Hermet *et al*. and predicted values for the bulk modulus of TiNiSn utilizing the Birch-Murnaghan equation of state (BM-EOS) as a model.[18] In a comparison study of the full-Heusler $TiNi_2Sn$ and half-Heusler TiNiSn, Hermet *et al*. compared the mechanical and structural properties of these materials based on the Young's, shear moduli and the bulk modulus for these materials.[30] To this date, there are no theoretical or experimental studies of the high-pressure thermoelectric and structural behavior of TiNiSn.

In this letter, we report the synthesis, high-pressure powder X-ray diffraction (HPXRD), high-pressure electrical and thermal measurements, density functional theory (DFT) calculations on TiNiSn, and an onset of a pressure-induced structural phase transition around 20 GPa to an orthorhombic structure described by space group *Cmcm* (No. 63). In the high-pressure electrical and thermal experiments, we have measured the electrical resistance, Seebeck coefficient, relative change in the thermal conductivity, and relative changes to the dimensionless figure of merit, ZT, of TiNiSn up to 3.5 GPa. A significant enhancement of the thermoelectric efficiency over this pressure range was observed.

The refined structural unit cell parameters for the cubic phase for TiNiSn are $a = b = c = 5.933$ (1) Å as determined by a Rietveld refinement performed on ambient pressure XRD data, Figure S1, which agrees well with the literature values.[22,31] This value is also in good agreement with the Generalized Gradient Approximation (GGA) calculations performed as part of this study. Atomic positions for all atom locations in the unit cell for the ambient cubic crystal structure described by the *F*-43*m* space group (No. 216) are fixed due to symmetry conditions. Figure 1 depicts the evolution of the XRD patterns with increasing pressure.

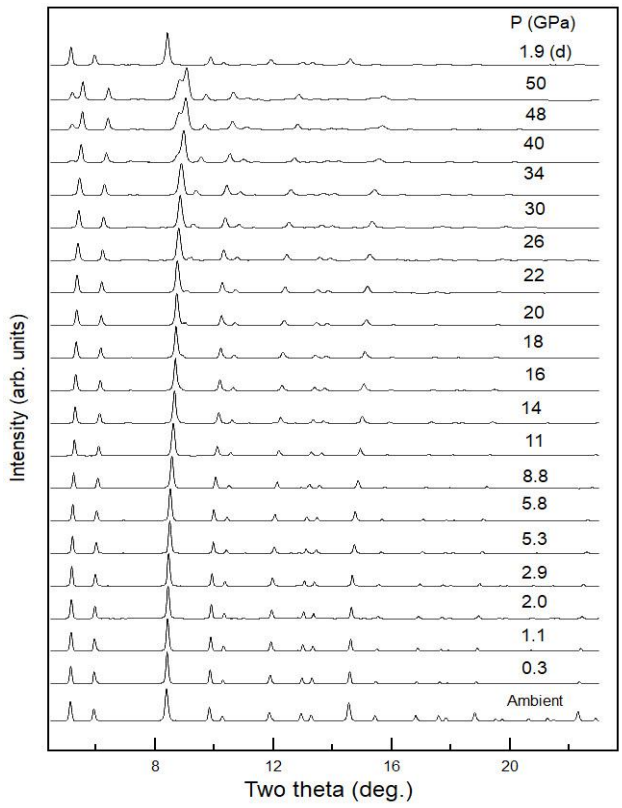

Figure 1. The evolution of XRD patterns with pressure increase for TiNiSn.

The expected shift to higher angles with increasing pressure is clearly visible over the entire pressure range. Below 20 GPa, the sample remains in the cubic structure and displays no

significant changes in the XRD patterns. Around 20 GPa, we have observed changes in the diffraction patterns. Low intensity peaks start to emerge around two theta angles 5.4°, 6.7°, 8.5° and 11.1°. The splitting of the diffraction peak around 8.5° is visible as a doublet since the diffraction line corresponding to the Ne pressure transmitting medium also merges with the sample peaks.[32] However, above 40 GPa, the intensity of the asymmetric shoulder peak to the left of the (220) peak increases in intensity significantly more prevalently as pressure is increased to 50 GPa. Figure 2 (a) shows the Lebail fitting for the low and high pressure phases. To elucidate other smaller XRD peaks that begin to emerge, Figure 2 (b) depicts the XRD patterns corresponding to 34, 40, 48, and 50 GPa separately to enhance the visibility of smaller XRD peaks.

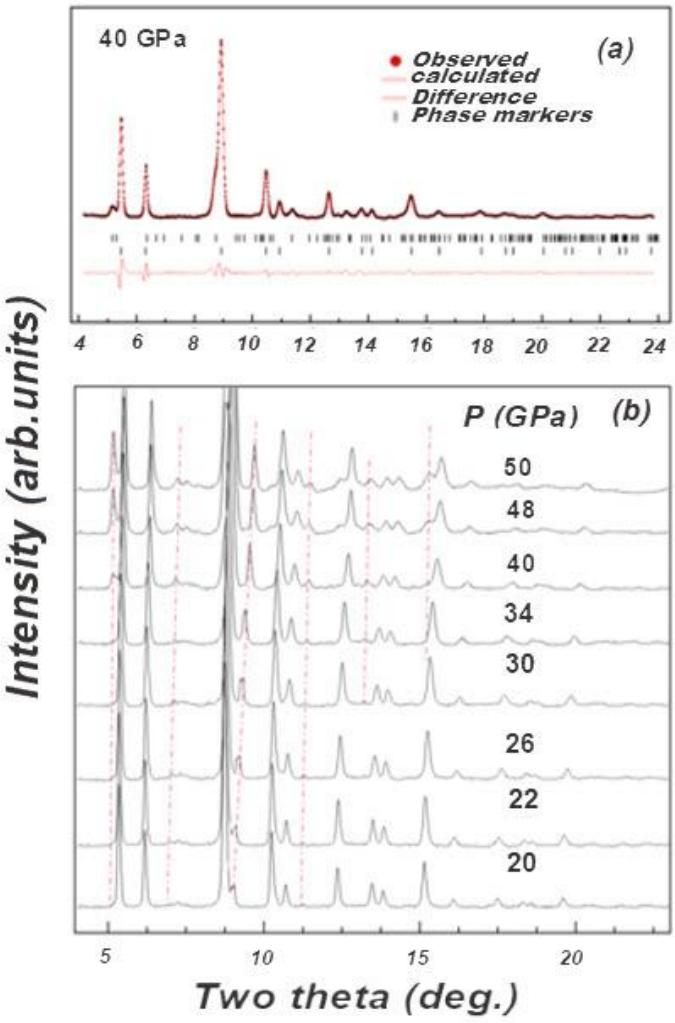

Figure 2 (a). Lebail analysis at 40 GPa showing the cubic structure described by *F*-43*m* space group and orthorhombic structure described by *Cmcm* space group. (b) The expanded view of XRD patterns from 20 to 50 GPa revealing appearance of several new peaks at 5.4°, 6.7°, and 11.1° corresponding to the high-pressure phase is shown. The peak at 8.5° is a doublet consisting of the neon PTM peak and a sample peak which becomes predominant at 50 GPa.

Elastic tensor analysis has been done to check mechanical stability in the investigated compound, TiNiSn. The calculated elastic tensor for the cubic system is given in Table S1. All the elastic constants are positive and satisfy Born's mechanical stability criteria.[33] The other elastic properties (e.g., elastic moduli and Debye temperature) are calculated using the Hill approximation.[34] The calculated bulk modulus is 130.78 GPa and the Poisson ratio is 0.27. This value of Poisson ratio indicates the ductile nature of TiNiSn. The Debye temperature is found to be 506.23 K, which has not been experimentally determined as of this publication. This is a very important parameter which links the thermodynamic properties to phonon-based properties.

The XRD patterns can be indexed well solely to the ambient pressure structureup to 20 GPa. In the pressure range of 20 GPa to 40 GPa, the XRD patterns reveal this structure remained as a major phase in addition to the evolving high pressure orthorhombic phase with space group *Cmcm* (No. 63). The high-pressure phase became prominent around 40 GPa. In order to obtain lattice parameters as a function of pressure, Lebail analysis was performed on each XRD pattern up to the maximal pressure.[35,36]

Once this analysis is performed on each XRD pattern corresponding to the entire pressure range for the ambient crystal structure, the lattice parameter, *a*, can be extracted and is displayed

in Table S2(a) alongside the calculated unit-cell volume, V. Even though the high-pressure phase starts to emerge around 20 GPa, the cell parameters (and V) can be obtained only above 30 GPa (for the high-pressure phase) and are shown in Table S2(b). Figure 3 shows a plot of V as a function of increasing pressure, which agrees well with the DFT calculations over the entire pressure range. The smooth decrease in V with compression indicates a reduction as expected for the TiNiSn sample.

To understand the mechanical properties of TiNiSn, the P-V data can be fit to the BM-EOS which allows determination of the bulk modulus. The BM-EOS is represented by the equation:

$$P(V) = \frac{3\,K_0}{2}\left[\left(\frac{V_0}{V}\right)^{\frac{7}{3}} - \left(\frac{V_0}{V}\right)^{\frac{5}{3}}\right]\left\{1 + \frac{3}{4}\left(K_0^{'} - 4\right)\left[\left(\frac{V_0}{V}\right)^{\frac{2}{3}} - 1\right]\right\} \quad (2)$$

where V_0 represents the zero-pressure volume, V represents the unit-cell volume, K_0 represents the bulk modulus, and K_0` represents the pressure derivative of the bulk modulus.[37]

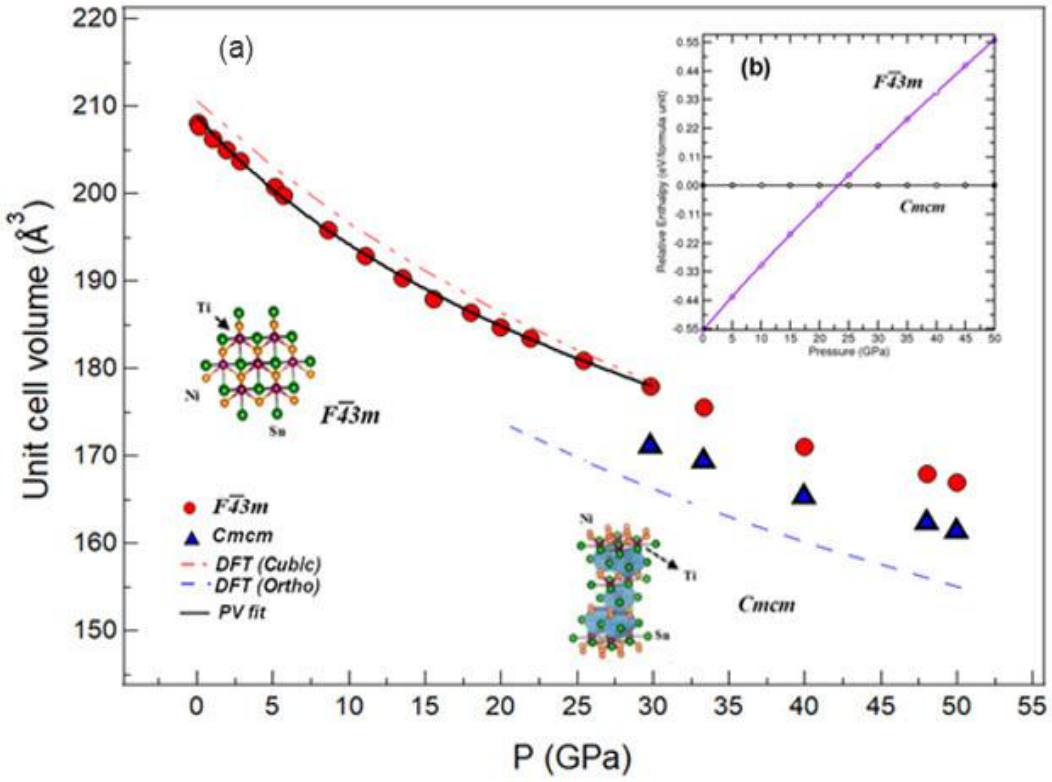

Figure 3. (a) Unit-cell volume as a function of increasing pressure for $\bar{F}43m$ and *Cmcm* phases (red circle and blue triangle represent experimental data, respectively). The solid line represents a fit to the 3rd-order Birch-Murnaghan equation of state (EOS) using experimental data. Density functional theory calculations (dotted lines). Insets (b) show enthalpy plot for low-pressure (*F*-43*m*) and high-pressure (*Cmcm*) crystal structures.

The initial volume parameter, was fixed to the ambient pressure value V_0 = 208.9 Å^3 determined from the lattice parameter extracted from the ambient pressure XRD pattern. This value agrees well with the values determined from DFT calculations of this study for GGA and Local-density approximation (LDA), 209.6 Å^3 and 196.1 Å^3, respectively. The optimized value of the bulk modulus from the fit to the 3rd-order BM-EOS is provided in Table S3 as K_0 = 106 (9) GPa. Additionally, from a modified version of Equation 2, the linear moduli for the *a*, *b*, and *c* axes

can be determined and are shown in Table S3(b) [Reference]. In the high-pressure phase, these moduli reveal an anisotropy between the *a* and *c* axes and the *b* axis. Specifically, the values of $M_{0,a}$ and $M_{0,c}$ are much more similar than $M_{0,b}$ indicating an anisotropy in compression strength where the *b* axis direction is softer than the *a* and *c* axes.

As no experimental reports on the bulk modulus of TiNiSn, no direct comparison can be made with experimental values. However, a recent experimental study was performed on a related half-Heusler TiCoSb and the bulk modulus was reported as 166 (6) GPa.[29] Additionally, a theoretical value for the bulk modulus for TiNiSn was reported by Wang *et al.* and Hermet *et al*. with values of 122 GPa and 120 GPa, respectively.[18,30] Furthermore, the DFT calculations performed as part of this study has determined as 130.8 GPa, which agrees quite well with the experimental value of 106 (9) GPa. Figure 3 (a) and (b) display the EOS determined both experimentally and by DFT calculation. Good agreement below 30 GPa in the lower pressure phase is clearly observed, and at elevated pressures as the phase becomes more mixed, there is some deviation between experiment and calculation. This deviation above 30 GPa is likely due to the experimental values being influenced due to the mixed phase state compared to the DFT calculation for the pure orthorhombic phase. The high-pressure structural search eventually lead to the cubic structure with *F*-43*m* space group with the lowest enthalpy in agreement with the experiment. Under pressure we could clearly see that an orthorhombic structure with *CmCm* space group, which becomes energetically more favorable around 20 GPa. This is in good agreement with the experimental observation.

We have used two different exchange-correlation functionals for full geometry optimization and found that the optimized parameters using GGA are in good accordance with experimental parameters. The electronic structure properties are shown in Figure 4 (a) and (b). From the plots,

it can be seen that TiNiSn is an indirect band gap semiconductor with a band gap of 0.46 eV. The existence of the valence band maxima at Γ – point and the conduction band minima at X – point is the evidence for the same. The band profile in the valence band region near the Fermi level is more flattened than those present in the conduction band. This difference in band dispersion motivated us to investigate the thermoelectric nature of the present compound which will be discussed in the next sections.

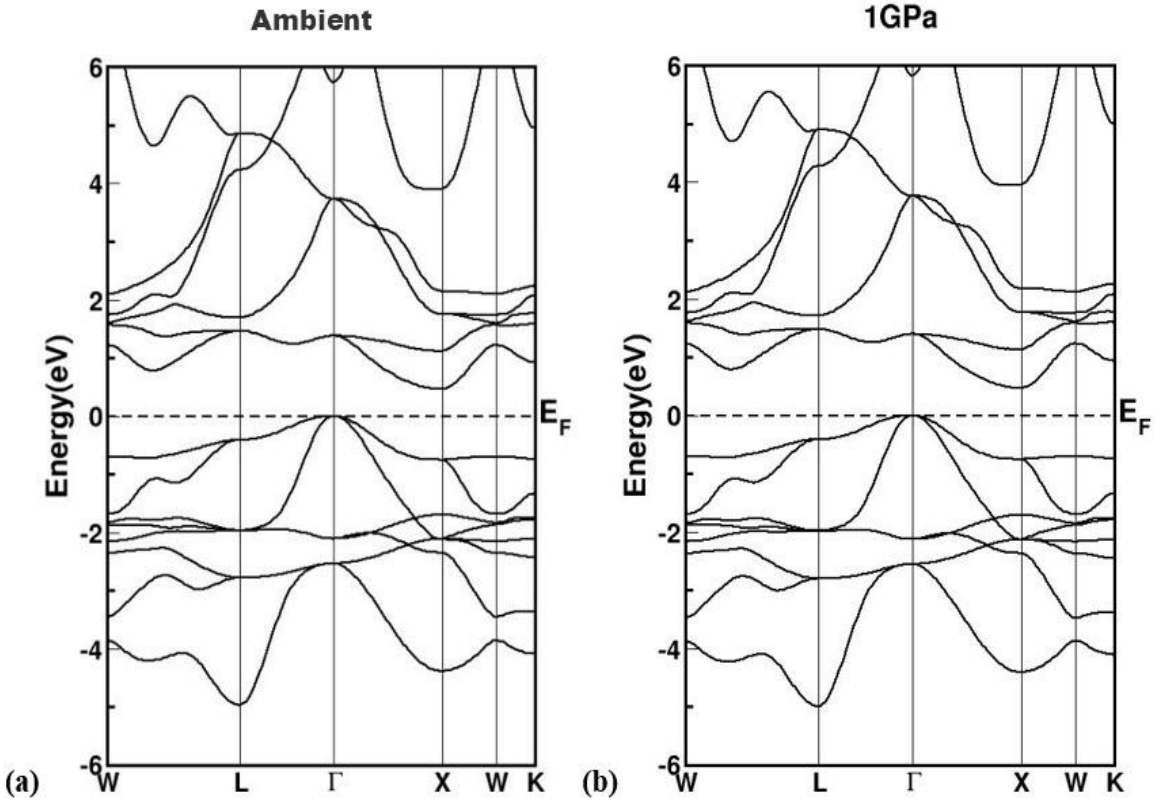

Figure 4. Calculated electronic band structure for TiNiSn at (a) ambient pressure and (b) 1 GPa.

All the thermoelectric properties are calculated under the relaxation time approximation. The calculated Seebeck coefficient for electrons is -334.28 μVK^{-1} at 100 K and the carrier concentration is around 10^{18} cm^{-3}. This value is in good accordance with the experimentally determined value of -339 μVK^{-1}. The electrical conductivity is of the order of 10^{17} $\Omega^{-1}m^{-1}s^{-1}$. The power factor ($\sigma\alpha^2$) can be determined from the electrical conductivity (σ) and Seebeck coefficient (α) which characterizes the energy that can be drawn from the system. Its value is on the order of 10^{10} $Wm^{-1}K^{-2}s^{-1}$. All the calculated TE properties can be correlated to the electronic structure through band dispersion. The combination of flat and dispersive bands has the effect on both the thermopower, and the electrical conductivity scaled by relaxation time.

Combining the experimentally determined electrical resistivity, Seebeck coefficient, and thermal conductivity measurements up to 3.5 GPa (details are in the SI), the ZT value for TiNiSn can be calculated as a function of pressure using Equation 1. Figure 5 shows the ZT normalized to the lowest pressure value as a function of increasing pressure. An overall increase in ZT is observed over the pressure range from 1 to 3 GPa which levels out as pressure is increased further to 3.5 GPa. The initial increase in ZT value over the pressure range from 1 to 3 GPa is almost 15%. This 15% increase is despite the large increase in the thermal conductivity of over 60%, and is likely due to the fairly large increase in the absolute value of the Seebeck coefficient over this same pressure range in addition to the electrical resistivity decrease. It is important to note that the thermoelectric measurements were performed under non-hydrostatic conditions and while this may affect the results, it does not appear to influence the results in our experiments.[38]

As reduction of the thermal conductivity through doping has been greatly explored for half-Heusler type alloys, further exploration of doped alloys of TiNiSn at high-pressure conditions may be interesting to pursue. Nonetheless, measuring the properties of the pure TiNiSn alloys for an understanding of the pressure effect on the thermoelectric properties without distortions introduced through doping is important.

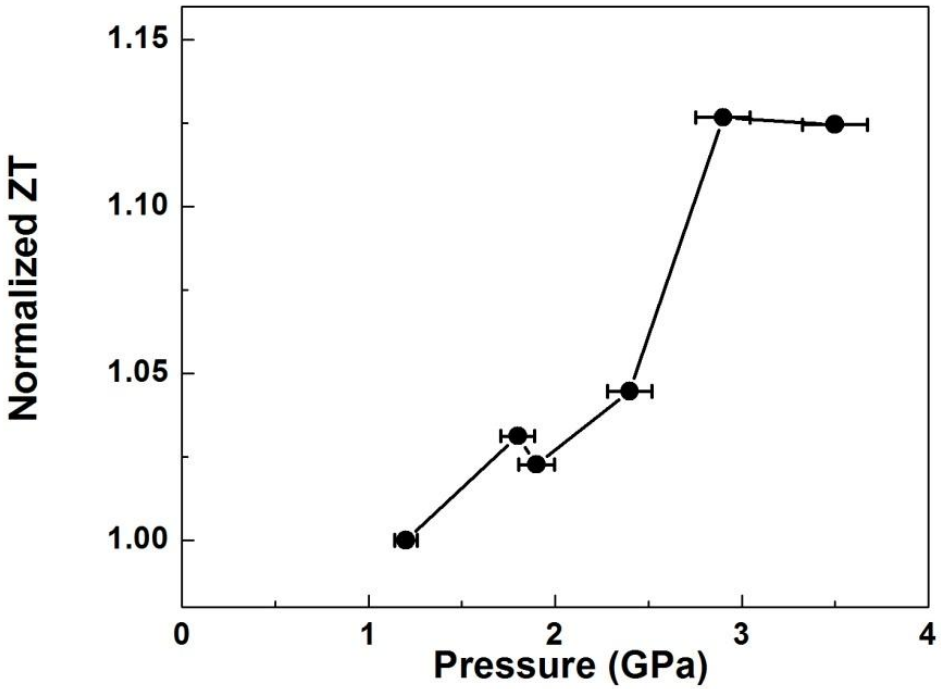

Figure 5. The dimensionless figure of merit ZT is plotted as a normalized value as a function of increasing pressure for TiNiSn. An increase of almost 15% is observed over the pressure range from 1 to 3.0 GPa with a plateau seemingly observed above 3.0 GPa.

In conclusion, we have performed HP-XRD and DFT calculations on TiNiSn up to 50 GPa and observed stability of the ambient crystal structure up to 20 GPa. Above 20 GPa, there are distinct indications of a pressure-induced secondary crystal phase developing as pressure increases

evidenced by the emergence of several new diffraction peaks. Utilizing structure searching techniques we have identified the high-pressure phase as an orthorhombic structure described by the *Cmcm* space group. The unit-cell volume as a function of pressure was fit to a 3rd-order BM-EOS yielding a bulk modulus value of 106 (9) GPa which agrees with the DFT calculations performed (130.8 GPa). Measurements of the thermoelectric properties at high-pressure conditions from 1 to 3.5 GPa were also presented for the first time. A 15% relative increase of ZT was observed with increasing pressure over the pressure range. The increase in thermoelectric efficiency of this material and the phase transition at high-pressure promises that future studies of this materials could be useful with chemical doping to establish further enhancement.

ACKNOWLEDGMENTS

Portions of this work was performed at HPCAT (Sector 16), Advanced Photon Source (APS), Argonne National Laboratory. HPCAT operations are supported by DOE-NNSA's Office of Experimental Sciences. The APS is a U.S. Department of Energy (DOE) Office of Science User Facility operated for the DOE Office of Science by Argonne National Laboratory under Contract No. DE-AC02-06CH11357. G. V acknowledge CMSD, University of Hyderabad for providing the computational facility. Portions of this work were performed under the auspices of the U.S. Department of Energy by Lawrence Livermore National Laboratory under contract DE-AC52-07NA27344.

REFERENCES

(1) Sagotra, A. K.; Errandonea, D.; Cazorla, C. Mechanocaloric Effects in Superionic Thin Films from Atomistic Simulations. *Nature Communications* 2017, 8, 963.

(2) Schmidt, G. R.; Wiley, R. L.; Richardson, R. L. NASA's Program for Radioisotope Power System Research and Development. *AIP Conf. Proc.* 2005, 746, 429-436.

(3) Huang, L.; Zhang, Q.; Yuan, B.; Lai, X.; Yan, X.; Ren, Z. Recent Progress in Half-Heusler Thermoelectric Materials. *Mater. Res. Bull.* 2016, 76, 107-112.

(4) Poon, S.J.; Wu, D.; Zhu, S.; Xie, W.; Tritt, T. M.; Thomas, P.; Venkatasubramanian, R. Half-Heusler Phases and Nanocomposites as Emerging High-ZT Thermoelectric Materials. *J. Mater. Res.* 2011, 26, 2795-2802.

(5) Liu, W. S.; Yan, X.; Chen, G.; Ren, Z. F. Recent Advances in Thermoelectric Nanocomposites. *Nanomater. Energy* 2012, 1, 42-56.

(6) Xie, W.; Weidenkaff, A.; Tang, X. F.; Zhang, Q. J.; Poon, J.; Tritt, T. M. Recent Advances in Nanostructured Thermoelectric Half-Heusler Compounds. *Nanomaterials* 2012, 2, 379-412.

(7) Chen, S.; Ren, Z. F. Recent Progress of Half-Heusler for Moderate Temperature Thermoelectric Applications. *Mater. Today* 2013, 16(10), 387-395.

(8) Bos, J. W. G.; Downie, R. A. Half-Heusler Thermoelectrics: a Complex Class of Materials. *J. Condens. Mater.* 2014, 26, 433201.

(9) Zhu, T.; Fu, C.; Xie, H.; Liu, Y.; Zhao, X. High Efficiency Half-Heusler Thermoelectric Materials for Energy Harvesting. *Adv. Energy Mater.* 2015, 5, 1500588.

(10) Rogl, G.; Grytsiv, A.; Failamani, F.; Hochenhofer, M.; Bauer, E.; Rogl, P. Attempts to Further Enhance ZT in Skutterudites via Nano-Composites. *J. Alloy. Compd.* 2017, 695, 682–696.

(11) Shi, X.; Yang, J.; Salvador, J.; Chi, M.; Cho, J. Y.; Wang, H.; Bai, S.; Yang, J.; Zhang, W.; Chen, L. Multiple-Filled Skutterudites: High Thermoelectric Figure of Merit Through Separately Optimizing Electrical and Thermal Transports. *J. Am. Chem. Soc.* 2011, 133(20), 7837–7846.

(12) Zhao, L. D.; Hao, S.; Lo, L. H.; Wu, C. I.; Zhou, X.; Lee, Y.; Li, H.; Biswas, K.; Hogan, T. P.; Uher, C. *et.al.,* High Thermoelectric Performance via Hierarchical Compositionally Alloyed Nanostructures. *J. Am. Chem. Soc.* 2013, 135(19), 7364–7370.

(13) Lee, Y.; Lo, S. H.; Androulakis, J.; Wu, C. I.; Zhao, L. D.; Chung, D. Y.; Hogan, T. P.; Dravid, V. P.; Kanatzidis, M. G. High-Performance Tellurium-Free Thermoelectrics: Allscale Hierarchical Structuring of P-Type PbSe-MSe Systems (M = Ca, Sr, Ba). *J. Am. Chem. Soc.* 2013, 135(13), 5152–5160.

(14) Pei, Y. L.; Liu, Y. Electrical and Thermal Transport Properties of Pb-Based Chalcogenides: PbTe, PbSe, and PbS. *J. Alloy. Compd.* 2012, 514, 40–44.

(15) Twaha, S.; Zhu, J.; Yan, Y.; Li, B. A Comprehensive Review of Thermoelectric Technology: Materials, Applications, Modelling, and Performance Improvement. *Renew. Sustain. Energy Rev.* 2016, 65, 698-726.

(16) Nozariasbmarz, A.; Agarwal, A.; Coutant, Z. A.; Hall, M. J.; Liu, J.; Liu, R.; Malhotra, A.; Norouzzadeh, P.; Öztürk, M. C *et.al.,* Thermoelectric Silicides: A Review. *Jpn. J. Appl. Phys.* 2017, 56, 05DA04.

(17) Tobola, J.; Pierre, J.; Kaprayk, S.; Skolozdra, R. V.; Kouacou, M. A. Crossover from Semiconductor to Magnetic Metal in Semi-Heusler Phases as a Function of Valence Electron Concentration. *J. Phys. Condens. Matter* 1998, 10, 1013.

(18) Wang, L. L.; Miao, L.; Wang, Z. Y.; Wei, W.; Xiong, R.; Liu, H. J.; Shi, J.; Tang, X. F. Thermoelectric Performance of Half-Heusler Compounds TiNiSn and TiCoSb. *J. Appl. Phys.* 2009, 105(1), 013709.

(19) Bhattacharya, S.; Pope, A. L.; Littleton IV, R. T.; Tritt, T. M. Effect of Sb Doping on the Thermoelectric Properties of Ti-Based Half-Heusler Compounds, $TiNiSn_{1-x}Sb_x$. *Appl. Phys Lett.* 2006, 77, 2476-2478.

(20) Hohl, H.; Ramirez, A. P.; Goldmann, C.; Ernst, G.; Wölfing, B.; Bucher, E. Efficient Dopants for ZrNiSn-Based Thermoelectric Materials. *J. Phys. Condens. Matter*. 1999, 11, 1697-1710.

(21) Kurosaki, K.; Maekawa, T.; Muta, H.; Yamanaka, S. Effect of Spark Plasma Sintering Temperature on Thermoelectric Properties of (Ti,Zr,Hf)NiSn Half-Heusler Compounds. *J. Alloys Compds.* 2005, 397, 296-299.

(22) Hohl, H.; Ramirez, A. P.; Kaefer, W.; Fess, K.; Thurner, Ch; Kloc, Ch.; Bucher, E. A New Class of Materials with Promising Thermoelectric Properties: MNiSn (M = Ti, Zr, Hf). *Mater. Res. Soc. Symp. Proc.* 1997, 478, 109.

(23) Sakurada, S.; Shutoh, N. Effect of Ti Substitution on the Thermoelectric Properties of (Zr,Hf)NiSn Half-Heusler Compounds. *Appl. Phys. Lett.* 2005, *86*, 082105.

(24) Uher, C.; Yang, J.; Morelli, D. T.; Mesiner, G. P. Transport Properties of Pure and Doped MNiSn (M=Zr, Hf). *Phys. Rev. B* 1999, 59, 8615.

(25) Ovsyannikov, S.V., Shchennikov, V.V. "Pressure-Tuned Colossal Improvement of Thermoelectric Efficiency of PbTe." *Appl. Phys. Lett.* 2007, 90, 122103.

(26) Baker, J.; Kumar, R.; Park, C.; Kenney-Benson, C.; Cornelius, A.; Velisavljevic, N. Giant Pressure-Induced Enhancement of Seebeck Coefficient and Thermoelectric Efficiency in SnTe. *ChemPhysChem*. 2017, 18, 3315-3319.

(27) Baker, J.; Kumar, R.; Park, C.; Kenney-Benson, C.; Cornelius, A.; Velisavljevic, N. High-Pressure Seebeck Coefficients and Thermoelectric Behaviors of Bi and PbTe Measured Using a Paris-Edinburgh Cell. *J. Synchrotron Rad.* 2016, 23, 1368-1378.

(28) Zhao, L. D.; Lo, S. H.; Zhang, Y.; Sun, H.; Tan, G.; Uher, C.; Wolverton, C.; Dravid, V. P.; Kanatzidis, M. G. Ultralow Thermal Conductivity and High Thermoelectric Figure of Merit in SnSe Crystals. *Nature* 2014, 508, 373-377.

(29) Baker, J. L.; Kumar, R.; Park, C.; Velisavljevic, N.; Cornelius, A. Compressibility and Thermoelectric Behavior of TiCoSb Half-Heusler Compound at High Pressures. *Intermetallics* 2018, 95, 137-143.

(30) Hermet, P.; Niedziolka, K.; Jund, P. A First-Principles Investigation of the Thermodynamic and Mechanical Properties of Ni-Ti-Sn Heusler and Half-Heusler Materials. *RSC Adv.* 2013, *3*, 22176- 22184.

(31) Jeitschko, W. Transition metal stannides with MgAgAs and $MnCu_2Al$ type structure. *Metallurgical Transactions*. 1970, *1*, 3159.

(32) Hemley, R. J.; Zha, C. S.; Jephcoat, A. P.; Mao, H. K.; Finger, L. W.; Cox, D. E. X-Ray Diffraction and Equation of State of Solid Neon to 110 GPa. *Phys. Rev B* 1989, *39*, 11820.

(33) Mouhat, F.; Coudert, F-X. Necessary and Sufficient Elastic Stability Conditions in Various Crystal Systems. *Phys. Rev. B* 2014, 90, 224104.

(34) Hill, R. The Elastic Behavior of a Crystalline Aggregate. *Proc. Phys. Soc. Sect. A* 1952, 65, 349.

(35) Le Bail, A. Whole Powder Pattern Decomposition Methods and Applications: A Retrospection. *Powder Diffraction*. 2005, *20:4*, 316–326.

(36) Le Bail, A. Extracting Structure Factors from Powder Diffraction Data by Iterating Full Pattern Profile Fitting, in: Accuracy in Powder Diffraction II. *NIST Special Publication*. 1992, 846.

(37) Birch, F. The Effect of Pressure Upon the Elastic Parameters of Isotropic Solids, According to Murnaghan's Theory of Finite Strain, *J. Appl. Phys*. 1938, 9 279.

(38) Morozova, N. V.; Korobeinikov, I. V.; Ovsyannikov, S. V. Strategies and Challenges of High-Pressure Methods Applied to Thermoelectric Materials, *J. Appl. Phys*. 2019, 125, 220901.